Original Article

Design and optimization of circularly polarized dielectric resonator antenna array based on Al_2O_3 ceramic

Hao Pan [a,b,1], Yu-Peng Li [a,1], Hai-Feng Zhang [a,*]

[a] *College of Electronic and Optical Engineering & College of Flexible Electronics (Future Technology), Nanjing University of Posts and Telecommunications, Nanjing, 210023, China*
[b] *Department of Physics in College of Science, City University of Hong Kong, Hong Kong, China*

A B S T R A C T

A comprehensive design of an ultra-broadband circularly polarized (CP) dielectric resonator antenna (DRA) array operating in the C-band for fifth-generation (5G) communication systems is presented in this paper. The objective is to achieve a compact antenna size capable of receiving and transmitting CP electromagnetic waves over a wider bandwidth. The material chosen for the dielectric resonator (DR) is Alumina (Al_2O_3) ceramic, known for its low dielectric loss and exceptional mechanical properties, making it an ideal candidate for the DR. The proposed design utilizes a 2 × 2 array of cross-shaped DRs, fed by a compact circular phase-shift feeding network with double-point feeding. This configuration results in a 3-dB axial ratio (AR) bandwidth of 48.7 % and an impedance matching bandwidth (IMB) of 53.2 %. The antenna's horizontal size is reduced to $1.17 \times 1.17 \lambda_0^2$, and the gain is significantly enhanced by exciting multiple Mie resonances in the stacked DRs, yielding a measured peak gain of 12.48 dBic. These outstanding features position the CP DRA array as an excellent choice for 5G communication systems.

1. Introduction

The exponential advance of mobile internet and internet of things for 5G communication is bringing abundant data exchange and extremely harsh requirements for the high data rates and capacity [1–4], which is also challenging for the antenna in the 5G wireless system. Meanwhile, the C-band (4.8–5 GHz) has been regarded as one of the operating bands of 5G communication in China. Therefore, the corresponding antennas for such an application are required to possess a wider IMB, higher gain, and better CP performance to overcome the high power loss and attenuation of the electromagnetic wave in the propagation. Currently, the microstrip patch antenna (MPA) is one type of the most common antenna in 5G systems depending on the lightweight, low cost, and easier installation. However, the large metallic loss, the restrict requirements of low matching tolerance in the high-frequency band, and narrow IMB still greatly limit the further practical application of MPA [5,6]. Therefore, it is a crucial issue to tailor one new-type antenna with a wider IMB, excellent CP performance, and higher gain to replace the MPA for the 5G communication system.

The dielectric resonator (DR) antenna (DRA) had attracted much

attention depending on its favorable features of compactness, low loss, wide IMB, high radiated efficiency, design flexibility, etc [7]. Owing to the absence of conduction losses and surface waves, the DRAs can achieve the radiation efficiency of above 90 % in the microwave band. Meanwhile, various choices of permittivity ranging from 6 to 140 S/m and multiple operating modes of DRs benefit the design flexibility of DRAs and extend the IMB [8]. In addition, the electromagnetic wave can radiate from all sides of DRA except for the grounding plate in comparison to both radiated crevices of MPA, thus also resulting in a wider operating bandwidth. The quality factor Q of DR, an important factor affecting the working bandwidth of DRA, can be reduced to improve IBM of DRA at a single resonant mode by adopting the DR with a lower permittivity. As permittivity is lower than 10 S/m, the IMB of DRAs can reach a maximum of 20 % with further optimization [9]. Meanwhile, inducing multiple resonant modes in DR is also an effective way to extend the operating band, e.g., Li and his researchers designed a rectangular DRA with an IMB of over 40 % by exciting the TE111 and TE113 modes simultaneously [10].

In the current 5G communication system, the CP DRA is usually preferred relying on its several attractive features, e.g., the strong
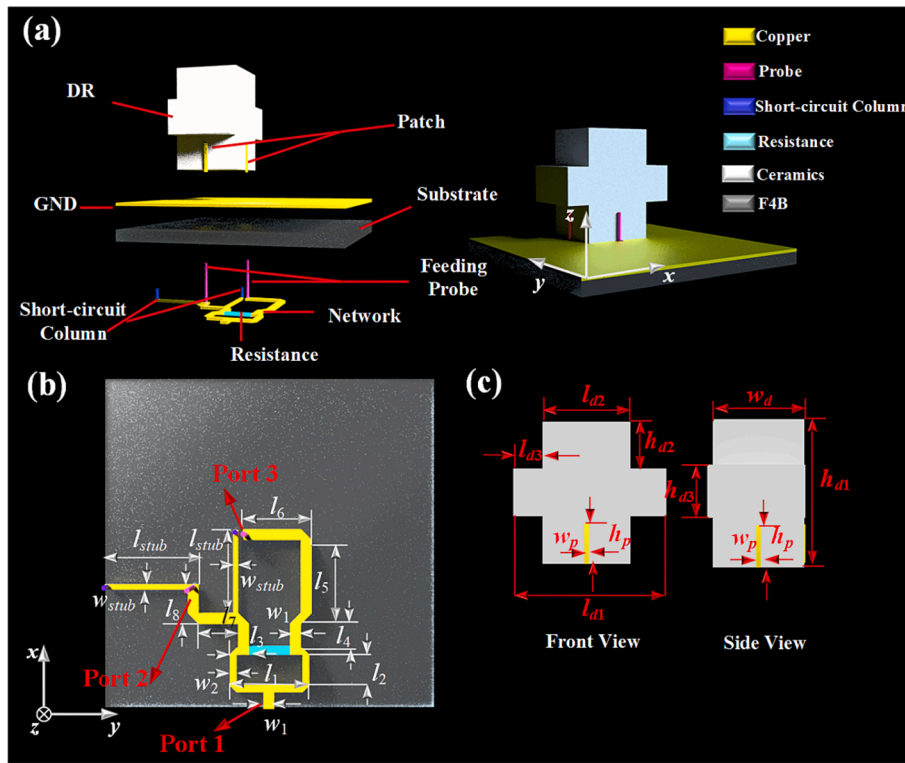

Fig. 1. The schematic of configuration of CP DRA. (a) The perspective view and detailed structures of the proposed CP DRA. (b) The detailed configuration and sizes of feeding network. (c) The construction of the proposed cross-shaped DR and detailed sizes.

independence of antenna orientation between the transmitter and receiver, high reflectivity, high absorption, less weather disturbance, and suppression of multi-path effect as compared to linearly polarized (LP) DRA, thus widely used in copious communication systems, e.g., satellite communication systems, mobile communication systems, navigation systems and radar systems, etc [11,12]. To acquire excellent CP radiation for the DRA, many different methods have been adopted to induce the orthogonal modes, e.g., modifying the DR structures and utilizing the special feeding techniques. The different perturbation DR structures, such as chamfered [13], cruciform [14], semicircular [15], inverted-pyramid [16], inverted-sigmoid shaped [17], circular-sectored [18], double-C-shaped configuration [19] etc., can be fed by the cross-shaped slot [20], Y-shaped [21] and helix [22] microstrips, etc, to induce the orthogonal modes for CP radiation, which can be called the single-point-feeding DRA. Although the single-point-feeding DRAs possess the advantage of simplicity and flexibility of design, the 3-dB axial-ratio (AR) bandwidth of these DRAs only ranging from 1% to 15% still greatly restricted the further practical applications.To acquire better CP performance in a wider band, multiple-point feeding structures have been adopted [23–29]. Lim and Leung investigated a CP hollow rectangular DRA based on the underlaid quadrature coupler to achieve the 3-dB AR bandwidth of 33.8% [23]. Han *et al.* introduced a novel hybrid 4-point feeding network to excite the rectangular DR, which can realize the 3-dB-AR bandwidth of 54.1% [27]. Kumar *et al.* presented a wide-band CP broadside radiation characteristics by using stacked rectangular DRA with different volumes [30]. However, the low gain of the single CP DRAs mentioned above still narrowed the application field. Although the configuration, e.g., horn [33], EBG [34], etc., can greatly improve the antenna gain, they also result in the larger size and enhances the complexity, thus leading to the decrease of practical value. By comparison, constructing the CP DRA array, which mainly depends on the phase sequential feeding network, is a significant choice to break through the limitations of low gain while maintaining the simple fabrication [35–43]. Sun *et al.* designed the 2×2 substrate-integrated cylindrical DRA array operating in the 60 GHz, which can acquire the gain of 11.43 dBic and 15.9% 3-dB-AR bandwidth based on the sequential rotation feeding method [39]. The Rad *et al.* presented a 2×1 dual-polarized DRA array with the measured gain of 9.6 dBic for X-band radar applications, which simultaneously attained the 3-dB-AR bandwidth of 23% and 30% for left-hand circularly polarized (LHCP) and right-hand circularly polarized (RHCP), respectively

[41]. Note that the CP performances of current DRA arrays with high gain are mainly focused on the narrow bandwidth due to the single method for CP realization, which becomes a bottleneck of practical application of DRA. Meanwhile, the expanded size of the DRA array with the increase of element number is also a crucial poser in the practical research of DRA especially for 5G communication system.

Alumina (Al2O3) ceramic is a significant ceramic material widely utilized in various fields such as electronics, aerospace, chemical engineering, medical, and mechanical engineering. It possesses a high dielectric constant typically ranging from 9 to 10 [42–44], enabling the fabrication of smaller-sized Al2O3 ceramic resonant antennas operating at higher frequencies. This characteristic is crucial for miniaturization and integration of wireless communication devices. Additionally, the low dielectric loss property of Al2O3 ceramic reduces energy loss during signal transmission [45], enhancing antenna performance and system transmission efficiency. Al2O3 ceramic also exhibits high temperature stability, excellent mechanical strength, rigidity, and corrosion resistance [46–48], enabling it to withstand special application scenarios, external impacts, vibrations, as well as resistance to chemical substances and humidity. Consequently, resonant antennas made of Al2O3 ceramic exhibit long-term stability and reliability in high-temperature environments, possess durability, and are resistant to corrosion in harsh conditions. These characteristics make Al2O3 ceramic an ideal material for manufacturing high-performance antennas, widely applied in communication, radio spectrum, satellite communication, radar systems, and other fields [49,50].

In this paper, an ultra-broadband CP DRA array based on Al2O3 ceramic working in the C-band for 5G communication is proposed. Al2O3 ceramic becomes an ideal material choice for DR due to its low dielectric loss and excellent mechanical properties. To acquire better CP performance for the DRA array, a series of feeding structures containing the circular phase-shift feeding network and double-point feeding configuration are adopted to feed the cross-shaped DRs, the stacking structure of which simultaneously improves the antenna gain. Meanwhile, the compact feeding network also shrinks the horizontal antenna size to $1.17 \times 1.17 \lambda_0^2$ (λ_0 is the wavelength at the lowest frequency). According to the measurement result, the given 2×2 DRA array can achieve the 3-dB-AR bandwidth of 48.7%, IMB of 53.2%, and peak gain of 12.48 dBic. Compared with other reported CP DRA arrays with the identical element number, the proposed DRA array in this work breaks the limitation of narrow CP bandwidth while attaining the higher gain, and the shrinking horizontal size can also contribute to the integration application. In addition, the 2×2 DRA array also can be regarded as the basic element to fabricate the DRA array with more elements based on the appropriate

Table 1
Properties of the DR (Al_2O_3 ceramic).

ε_r	9.5
Density (g/cm^3)	3.9
Flexural strength (Mpa)	340
Compressive strength (Mpa)	3600
Dielectric strength (KV/mm)	25
Thermal conductivity (W/mk)	27
Modulus of elasticity (Gpa)	380
Highest application temperature (°C)	1750

Table 2
The dimensions of proposed CP DRA (Unit: mm).

Double-point Feeding Network					DR			
l_1	l_2	l_3	l_4	l_5	l_{d1}	l_{d2}	l_{d3}	h_{d1}
9.55	3.725	2.6	3.7	10.1	21	12	4	13.5
l_6	l_7	l_8	l_{stub}	w_{stub}	h_{d2}	h_{d3}	h_p	w_p
8.25	4.75	4.75	9.6	0.7	6.5	6.5	5.4	0.6
w_1	w_2				w_d			
1.3	0.8				12			

feeding network, which can show better antenna performance, e.g., higher gain, wider CP bandwidth, etc., to satisfy the high requirements of 5G communication system.

This paper has been organized as follows. The design of units of the CP DRA based on a double-point feeding network is introduced in section II. The 2 × 2 CP DRA array fed by the compact circular phase-shift feeding network is described in section III, and the experimental verification has been presented in IV. Finally, section V provides the conclusion.

2. Design of CP DRA

2.1. Configuration

The proposed CP DRA contains the double-point feeding network, copper probes, substrate, ground plane, cross-shaped DR, and metallic patches, as depicted in Fig. 1(a). The F4B (the relative permittivity $\varepsilon_{r1} = 3$ and the loss tangent $\tan \delta_1 = 0.003$) is chosen as the substrate with a volume of 40 mm × 40 mm × 0.5 mm. The double-point feeding network and ground plane are printed on the bottom and top of the

substrate, respectively. Meanwhile, the short-circuit columns located at the network are inserted into the substrate to connect the feeding network and ground plane. To excite multiple Mie resonant modes to improve the antenna gain, the stacking cross-shaped DR made of the Al_2O_3 dielectric ceramic with the relative permittivity $\varepsilon_{r2} = 9.5$ and loss tangent $\tan \delta_2 = 0.003$ [32] is adopted to lay above the ground plane, as presented in Fig. 1(c). The 99 % Al_2O_3 ceramic sintered at high temperature (2050 °C) exhibits exceptional performance, as demonstrated in Table 1. Considering the high hardness of alumina ceramic material, the dielectric resonator (DR) fabrication process involves grinding, utilizing diamond grinding wheels as the preferred abrasive material. Furthermore, double copper probes with the diameter d and height h_p are adopted to excite the cross-shaped DR, and the metallic patches existing between the DR and probes are tailored to gain better impedance matching and CP performance. The proposed CP DRA feeding line is terminated to a 50 Ω SMA connector for signal transmission. The detailed sizes of such DRA have been listed in Table 2.
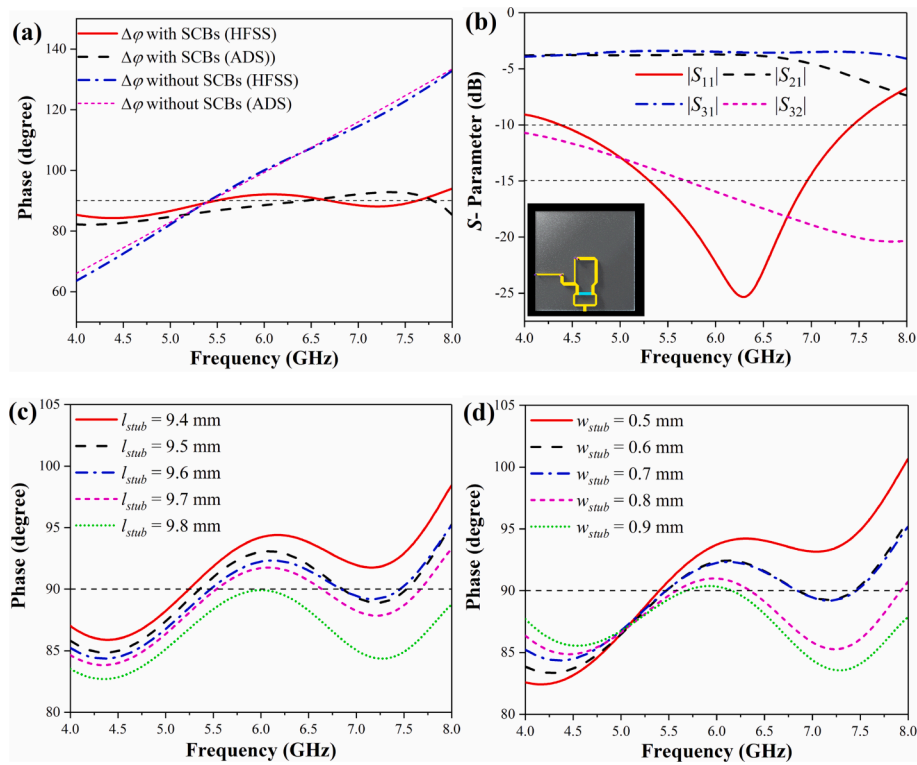
2.2. Double-point feeding network

To acquire better CP performance in a wider band, the double-point feeding network has been employed to excite the cross-shaped DR, as depicted in Fig. 1(b). The design of such a double-point feeding network must satisfy two principles to achieve wide-band CP radiation: equal-power division and 90° phase shift in a wider band. Therefore, the traditional Wilkinson power divider and novel 90° phase shifter have been introduced to the feeding network, whose equivalent circuit model is shown in Fig. 2. The Wilkinson power divider not only can effectively divide the equal power but also boost the isolation between two output ports, one of the basic guarantees for generating two independent LP waves. Simultaneously, the $\lambda_g/4$ (λ_g is the effective wavelength) microstrips connecting the input and output ports can achieve the impedance matching between different ports as Z_1 is equal to $2^{1/2}Z_0 = 70.6$ Ω ($Z_0 = 50$ Ω). In addition, the other part of the feeding network, the 90° phase shifter, can form a 90° phase difference between double-independent LP waves originating from the power divider. However, the traditional phase shifter cannot keep the stable phase difference in a wide operating band, which further affects the CP performance. Consequently, the 90° phase shifter with double short-circuit branches (SCBs) have been adopted to acquire the stable 90° phase difference in a wider bandwidth.

To theoretically verify the broadband phase stability of such an
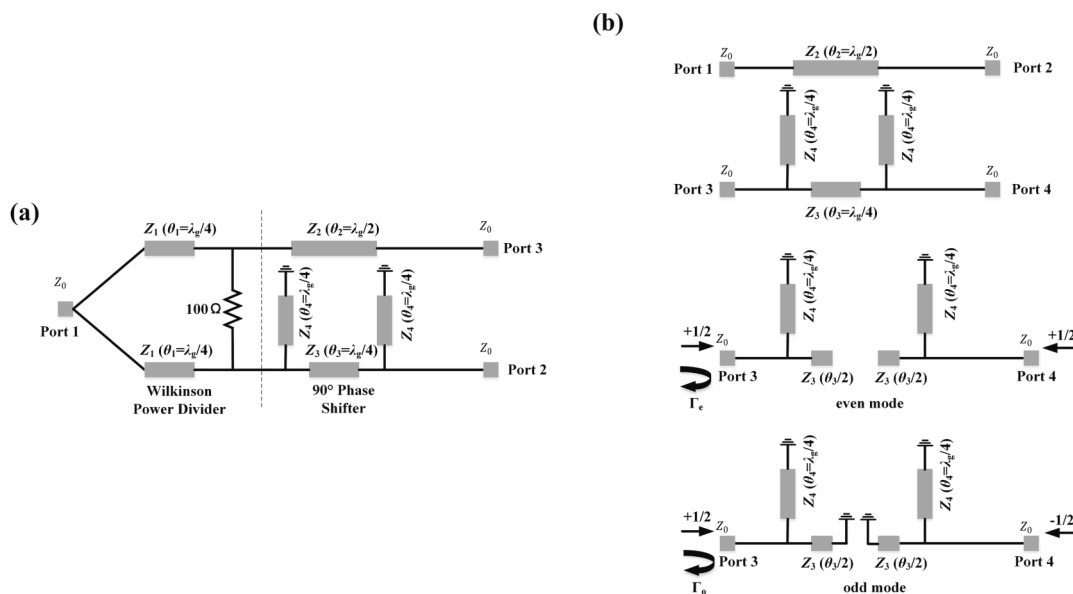
Fig. 2. (a) The schematic of equivalent circuit model of the double-point feeding network. (b) The diagrams and analysis of 90° phase shifter based on even and odd modes.

Fig. 3. (a) The phase difference between ports 2 and 3 in the double-point feeding network with or without the SCBs. (b) The scattering parameters of double-feeding network with SCBs. (c) The phase difference between ports 2 and 3 versus the length of SCBs l_{stub} at $w_{stub} = 0.7$ mm. (d) The phase difference between ports 2 and 3 versus the width of SCBs w_{stub} at $l_{stub} = 9.6$ mm.
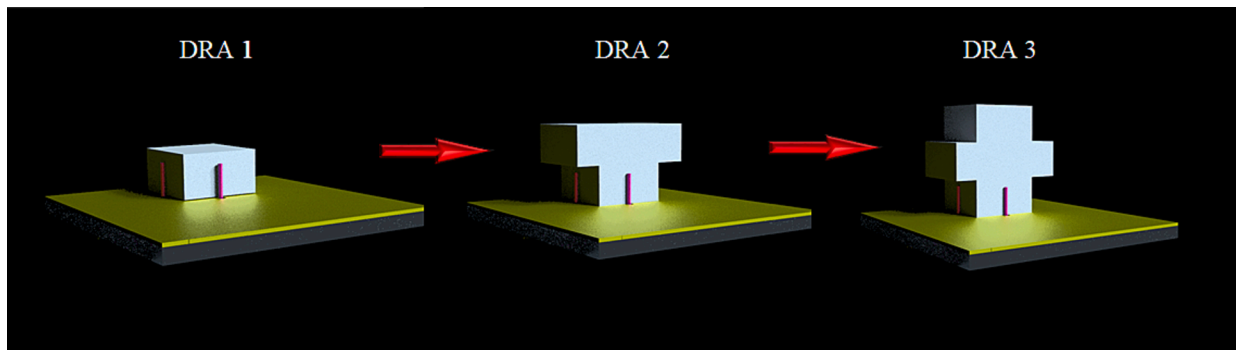
Fig. 4. The diagrams of the unit CP DRA evolution: DRA 1, DRA 2 and DRA 3.

exotic phase shifter with SCBs, the analysis based on the even/odd modes and superposition principle has been performed, as shown in Fig. 2(b). The scattering parameters and the phase difference between ports 2 and 4 have been given by the below formulas:

$$S_{11} = S_{22} = 0 \tag{1}$$

$$S_{33} = S_{44} = \frac{1}{2}\left(\frac{1 - jW_1}{1 + jW_1} + \frac{1 + jW_2}{1 - jW_2}\right) \tag{2}$$

$$S_{34} = S_{43} = \frac{1}{2}\left(\frac{1 - jW_1}{1 + jW_1} - \frac{1 + jW_2}{1 - jW_2}\right) \tag{3}$$

$$\Delta\varphi = \arg(S_{21}) - \arg(S_{43}) = -\theta(f) + \pi - \tan^{-1}\left(\frac{1 + W_1(f)W_2(f)}{W_1(f) - W_2(f)}\right) \tag{4}$$

where $W_1 = \overline{Y}_3\tan\left(\frac{\theta_3}{2}\right) - \overline{Y}_4\cot(\theta_4), W_2 = \overline{Y}_3\cot\left(\frac{\theta_3}{2}\right) - \overline{Y}_4\tan(\theta_4)$ with $\theta(f) = \pi\overline{f}, \theta_3(f) = \frac{\pi}{2}\overline{f}, \theta_4(f) = \frac{\pi}{2}\overline{f}$, the normalized frequency $\overline{f}$, and the central

frequency f_0. The $\overline{Y}_3$ and $\overline{Y}_4$ indicate the normalized characteristic admittance, respectively. As $\overline{Y}_3$ and $\overline{Y}_4$ are equal to 1 and 0.657, implying $Z_2 = Z_3 = Z_0 = 50\ \Omega$ and $Z_4 = 1.52Z_0 = 76\ \Omega$, and the reflection coefficient is below -15 dB, the calculated relative bandwidth of the 90° phase shifter ($|\varphi\text{-}90°| < 3°$) can reach 50 %.

Based on the theoretical analysis of the equivalent circuit model, the simulation of such a feeding network consisting of a Wilkinson power divider and 90° phase shifter has been performed by the commercial simulation softwares (Advanced Design System (ADS) and High Frequency Structure Simulator (HFSS)) to validate the theoretical analysis of phase stability and scattering parameters, which is presented in Fig. 1 (b). To clarify the improvement of the phase stability of the feeding network, the feeding networks with or without SCBs are investigated. It can be noted in Fig. 3(a) that as the traditional phase shifter (without SCBs) is adopted, the phase difference $\Delta\varphi$ (90°±3°) between double output ports is limited to the narrow bandwidth, 5.25–5.58 GHz (ADS) and 5.35–5.61 GHz (HFSS), which simultaneously varies linearly with
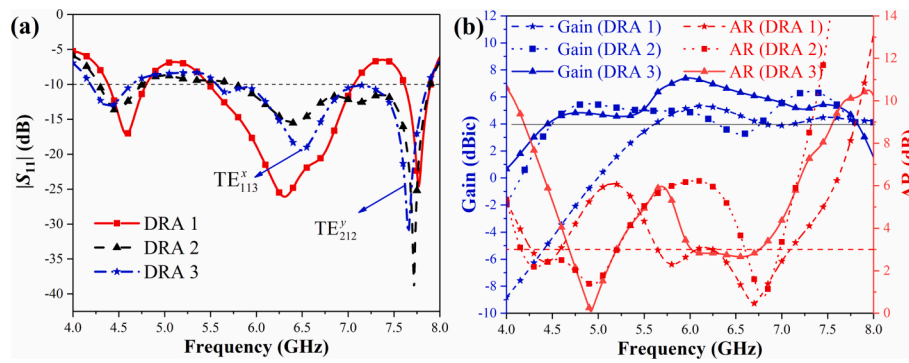
Fig. 5. The simulated electromagnetic performance of CP DRAs 1, 2 and 3. (a) Reflection coefficient $|S_{11}|$. (b) Gain and AR.
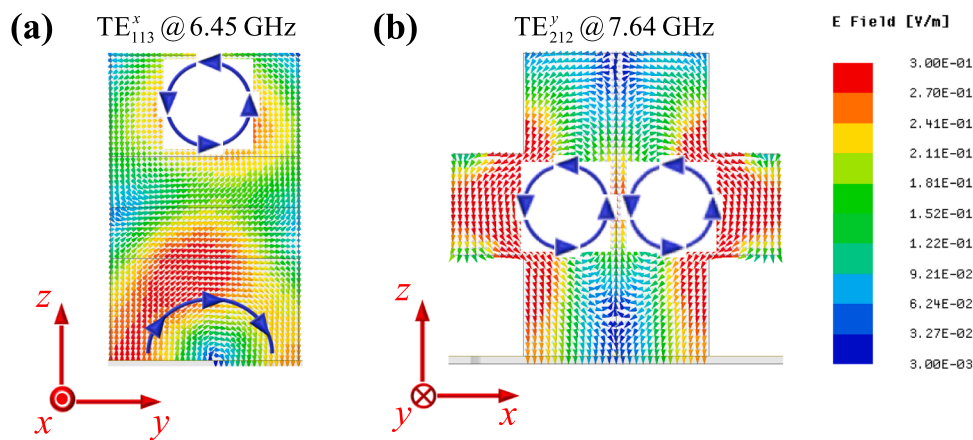

Fig. 6. The electric field of radiating modes in the isolated DR with ground plane and substrate extracted by the HFSS eigenmode solver.
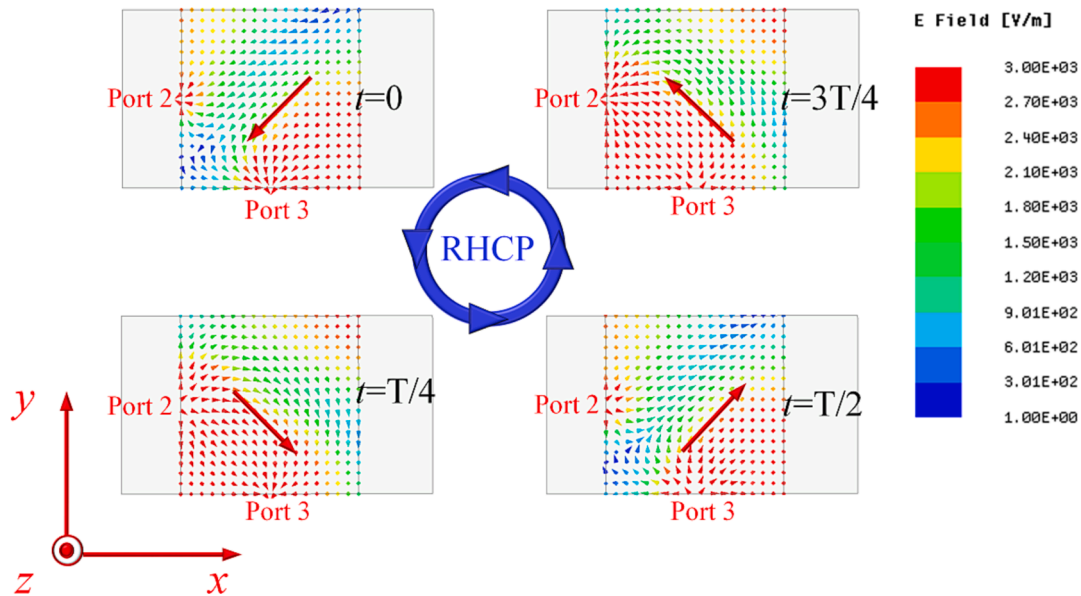

Fig. 7. The simulated electric-field distribution on the plane of DR perpendicular to the z-axis ($z = 4$ mm) in the proposed unit CP DRA 3 at different time instances of 6.4 GHz (T is the time period) based on HFSS driven-mode solver.

frequency. Combing double SCBs with the phase shifter, the feeding network can reach the stable phase difference $\Delta\varphi$ (90°±3°) at 5.56–7.94 GHz (ADS) and 5.06–7.9 GHz (HFSS), implying that the added SCBs can effectively contribute to the stability of phase difference in a wide band.

Meanwhile, it is worth noting in Fig. 3(b) that the proposed feeding network with the SCBs can acquire the lower reflection coefficient ($|S_{11}|<$-15 dB) at 5.3–7 GHz, where the transmission coefficients $|S_{21}|$ and $|S_{31}|$ are nearly close to −3.5 dB, according to the simulation results of HFSS. Therefore, the proposed double-point feeding networks with SCBs can form double independent LP waves with a phase difference of 90° to
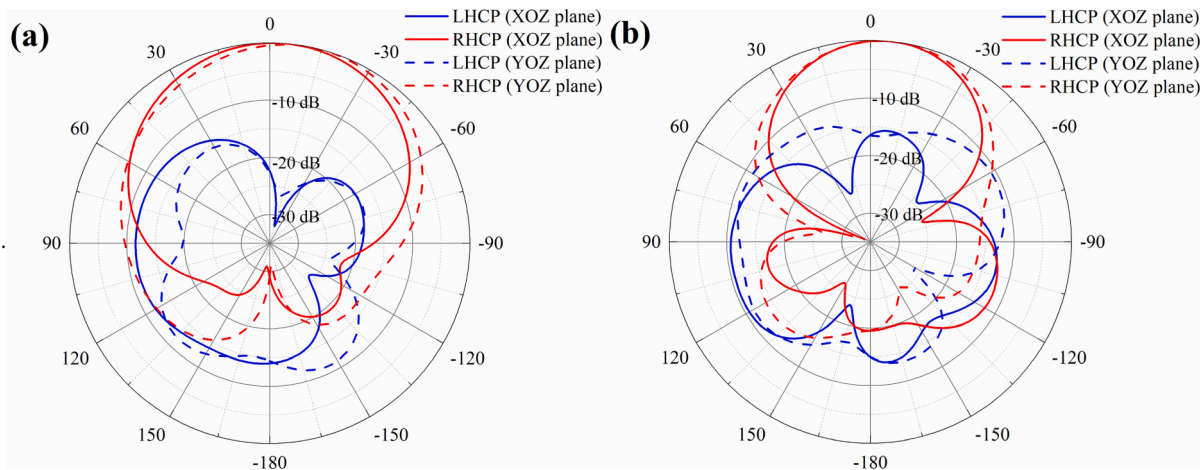
Fig. 8. The simulated normalized CP radiation patterns of DRA 3 in the XOZ and YOZ planes at some frequencies. (a) 4.9 GHz. (b) 6.5 GHz.
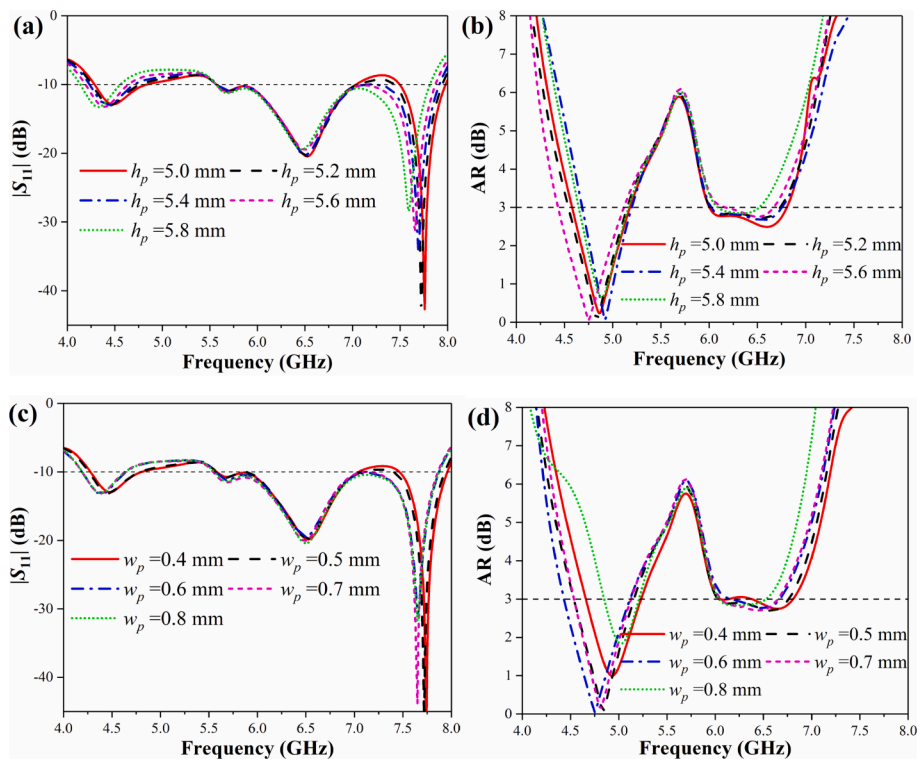

Fig. 9. The simulated reflection coefficient $|S_{11}|$ and AR of DRA 3 versus parasitic patches on the cross-shaped DR. (a) and (c) show the simulated $|S_{11}|$ versus h_p and w_p. (b) and (d) demonstrate the simulated AR versus h_p and w_p.

excite the cross-shaped DR. In addition, the length and width of SCBs are significant factors in tuning the stable-phase-difference band, as illustrated in Fig. 3(c) and (d). It can be seen that with the increase of length and width, the phase difference between double ports also raises in a wide band. As l_{stub} and w_{stub} are set as 9.6 mm and 0.7 mm, respectively, the phase difference can reach around 90° in the widest band, which best satisfies the requirement of the design of the following CP DRA.

2.3. Results and discussion of DRA

The aforementioned double-point feeding network with the phase difference of 90° in a wide band can provide double orthogonal-linear-polarized signals with the phase difference of 90° to excite the single DR, then radiating the circular-polarized waves composed of double

orthogonal-linear-polarized waves with the identical amplitude and the phase difference of 90° toward the far field. Therefore, the stable phase difference of 90° in a wide band between double ports in the feeding network can greatly enhance the CP performance of the single DRA based on the double-point feeding network. To explore the better electromagnetic characteristics (i.e., IMB, AR, and gain) of the single DRA, three different structures of DR (rectangular, T-shaped, and cross-shaped) are adopted as the radiated elements to fabricate three DRAs (shown in Fig. 4).

As depicted in Fig. 5, for DRA 1, the rectangular DR is fed by the double-point feeding network, which can achieve the IMB ($|S_{11}|<$-10 dB) of 4.4–4.8 GHz, 5.48–7.1 GHz, and 7.62–7.9 GHz, and the RHCP bandwidth (AR < 3 dB at $\theta = 0°$) of 4.28–4.6 and 5.65–7.1 GHz. Simultaneously, the 4-dBic antenna gain at $\theta = 0°$ for the DRA 1 can be
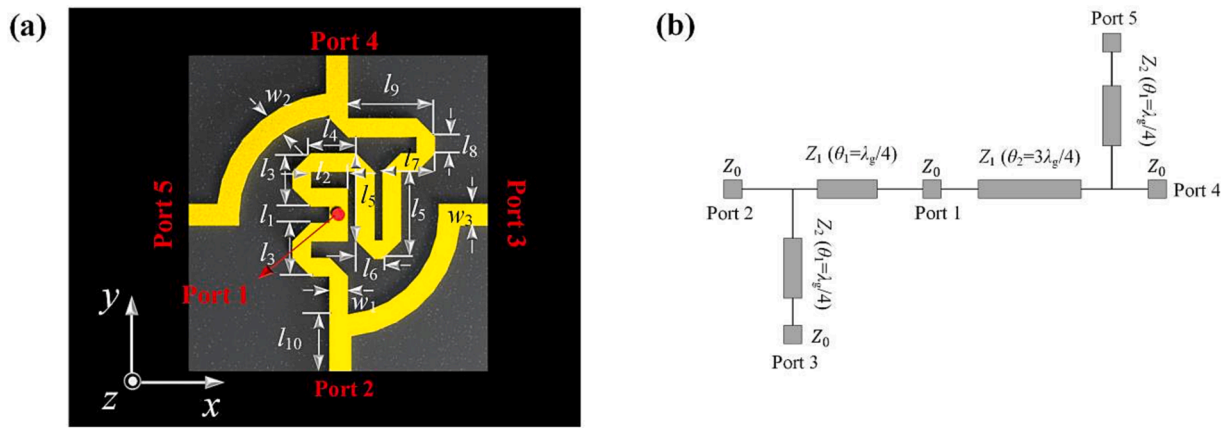
Fig. 10. (a) The schematic of compact circular phase-shift feeding network. (b) The simple equivalent circuit model of compact circular phase-shift feeding network: $Z_0 = 50\ \Omega$, $Z_1 = 54\ \Omega$, and $Z_2 = 59.14\ \Omega$.

Table 3
The dimensions of compact circular phase-shift feeding network (Unit: mm).

l_1	l_2	l_3	l_4	l_5	l_6	l_7
1	2.23	3.2	2.74	6.6	1.6	3.15
l_8	l_9	l_{10}	w_1	w_2	w_3	
1	5.25	2	1.1	0.85	1.3	

attained at 5.53–8 GHz and the peak gain can reach 5.32 dBic at 6.12 GHz. To further enhance the antenna gain in the lower band, since the resonance frequency is determined by the geometric dimensions and structure of the resonator, larger resonators can lead to changes in the resonance modes in the lower frequency range. Thus, a larger

rectangular DR with identical dielectric material is stacked on the one in DRA 1 to fabricate the DRA 2, which can induce the new Mie resonances in the lower frequency band.

According to the numerical calculation by HFSS, the simulated IMB of DRA 2 covers 4.3–4.75 GHz and 5.76–7.9 GHz, and the 3-dB AR bandwidth deteriorates thus decomposing into double narrow bands of 4.15–5.2 GHz and 6.6–6.7 GHz, which is blamed on the destruction of symmetry of the stacking DR. Moreover, the 4-dBic antenna gain bandwidth can extend to 4.5–6.3 GHz and 6.7–8 GHz, and the peak gain increases to 6.4 dBic at 7.3 GHz. The stacking effect alters the existing resonant conditions, thus, another rectangular DR is also stacked above the T-shaped DR in DRA 2 to induce another Mie resonances in the cross-shaped DR of DRA 3.

As depicted in Fig. 5, the DRA 3 can acquire the IMB of 4.2–4.64 GHz
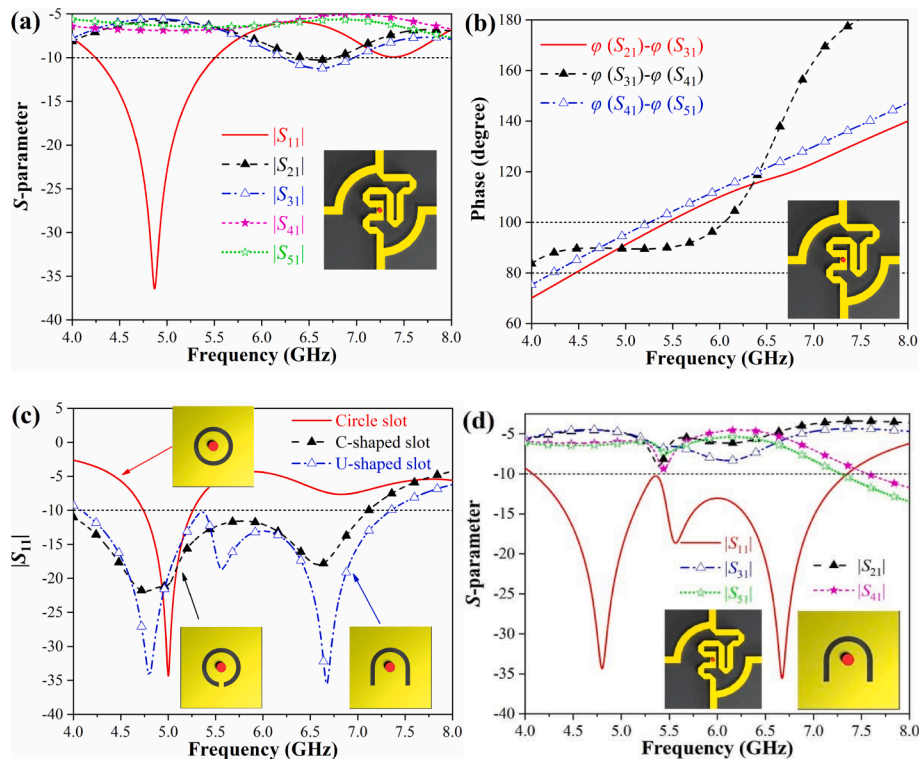
Fig. 11. The simulated scattering parameters and phase of the compact circular phase-shift feeding networks with or without slots as port 1 is excited. (a) The simulated scattering parameters of the feeding network without the etched slot. (b) The phase difference between the adjacent ports of the feeding network without the etched slot. (c) The reflection coefficients of feeding network with different etched slots. (d) The scattering parameters of the feeding network with the U-shaped slot.

Fig. 12. The structure of CP DRA array. (a) Perspective view of DRA array. (b) Vertical view of DRA array. (c) Back view of DRA array.
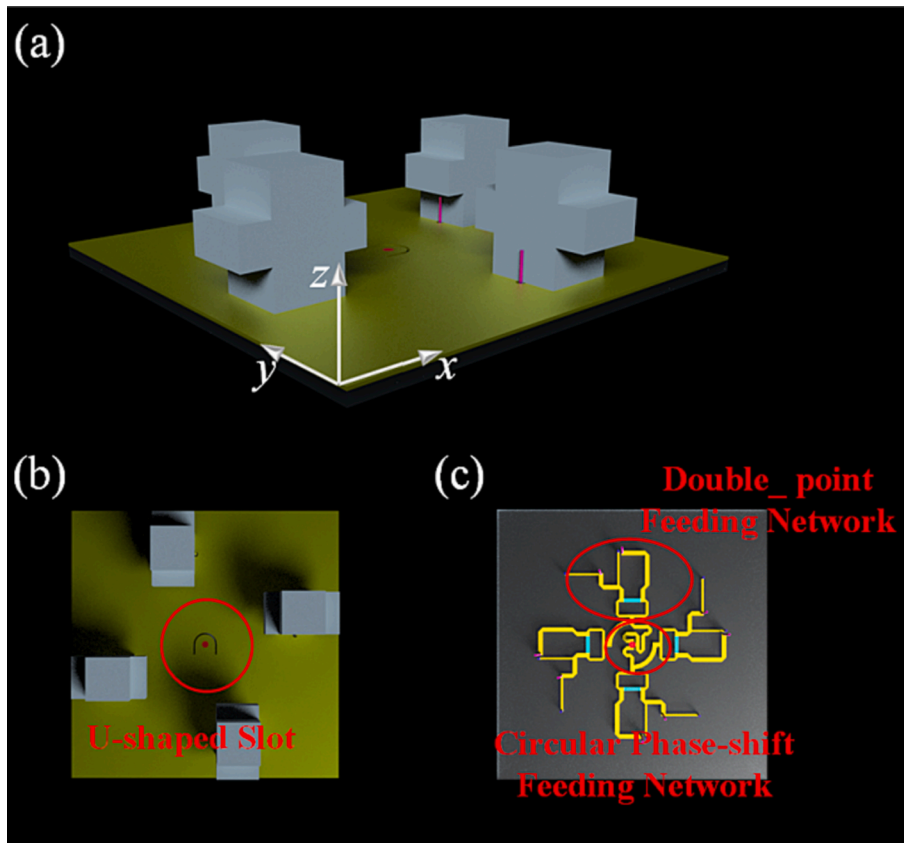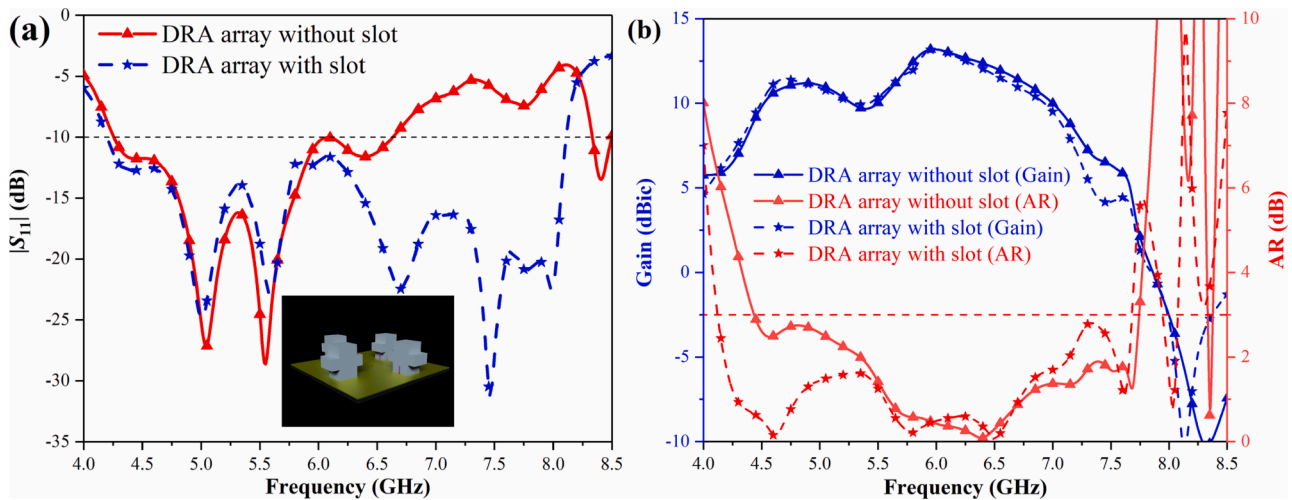

Fig. 13. The simulated performance of DRA array with/without the U-shaped slot on the ground. (a) Reflection coefficients $|S_{11}|$. (b) Gain and AR.

and 5.57–7.86 GHz, and the 3-dB AR bandwidth of 4.43–5.11 GHz and 6.16–6.68 GHz.

To further clarify the operating mechanism of DRA 3, the electric fields of radiated modes at 6.45 and 7.64 GHz are calculated by the HFSS eigenmode solver, as depicted in Fig. 6. Note that the radiated modes, TE^x_{113} and TE^y_{212}, are excited to further extend the IMB [51]. Meanwhile, the RHCP radiation of the proposed DRA 3 can be further demonstrated by the electric-field distribution in the cross-shaped DR as depicted in Fig. 7. Noted that as the time increases, the direction of electric-filed vectors at 6.4 GHz rotates in counterclockwise to ensure the RHCP radiation. Meanwhile, the simulated 4-dBic gain bandwidth of

DRA 3 is 4.45–7.82 GHz and the peak gain is improved to 7.4 dBic at 6 GHz. It can be noted that the maximum gain difference between DRA 2 and DRA 3 can reach 2.54 dBic in the operating band. Although the stacking structure of DR can greatly enhance the antenna gain in a wide band, the asymmetric cross-shaped configuration also deteriorates the CP performance thus attaining double narrow AR band, which is because that in the single DRA, two input orthogonal-linear-polarized signals supported by the double-point feeding network cannot excite double orthogonal-polarized radiation waves in the asymmetric cross-shaped DR, consequently not effectively radiating the circular-polarized wave.
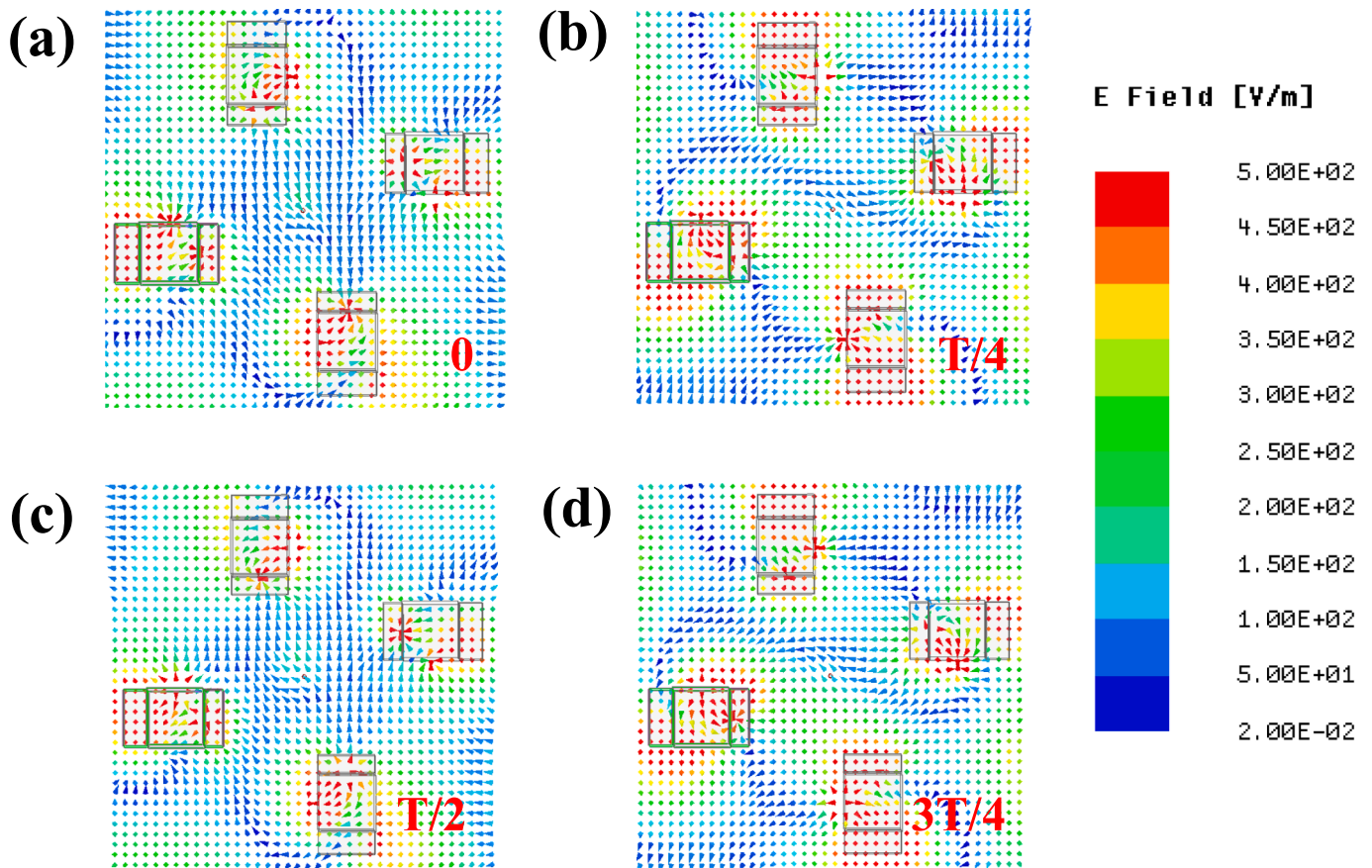
Fig. 14. The simulated electric-field distribution on the plane perpendicular to the *z*-axis containing all DRs at different time instances. (a) 0, (b) T/4, (c) T/2, and (d) 3 T/4 at the frequency of 4.5 GHz (T is the time period) based on HFSS driven-mode solver.

Fig. 8 illustrates the normalized radiation patterns versus the angle of DRA 3 in XOZ and YOZ planes at 4.9 GHz and 6.5 GHz, respectively. At 4.9 GHz, the RHCP fields are at least 22 dB higher than LHCP fields in the broadside direction ($\theta = 0°$). The angle of the broadside, where RHCP is achieved, extends to over 40° with a symmetric radiation pattern. At 6.5 GHz, the LHCP fields are 16 dB lower than RHCP fields in the broadside direction and the angle of the broadside where RHCP dominates over LHCP can reach 30°.

The height h_p and width w_p of conducting patches (shown in Fig. 1 (c)) existing between the feeding probes and DR have a effect on the impedance matching and CP performance of the DRA 3, which is depicted in Fig. 9. With the increase of h_p, the Mie resonance existing in the high-frequency shifts to a lower frequency (from 7.7 to 7.6 GHz), thus forming the continuous IMB (depicted in Fig. 9(a)). However, the CP performance deteriorates in the second CP bandwidth–the CP bandwidth shrinks from 0.82 to 0.46 GHz (presented in Fig. 9(b)). Similarly, the increase of the width w_p also improves the impedance matching performance in a wider continuous band (shown in Fig. 9(c)), but worsens the CP performance (illustrated in Fig. 9(d)). Considering the comprehensive effect of h_p and w_p, the optimized height and width of the conducting patches are selected as 5.4 mm and 0.6 mm.

3. Design of CP DRA array

To improve the CP performance of the single DRA 3, the compact circular phase-shift feeding network is first tailored to connect four unit DRAs mentioned above, thus fabricating the rotational-symmetric 2 × 2 DRA array, namely the adjacent DRs perpendicular to each other. Owing to the 90° phase difference between the adjacent ports of the circular phase-shift feeding network, the phase of eight output ports in the feeding network consisting of circular and double-point feeding networks can reach 0°, 90°, 90°, 180°, 180°, 270°, 270°, and 360°, consequently exciting many pairs of orthogonal-linear-polarized waves with the identical amplitude and 90° phase difference to fabricate the circular radiation waves. Therefore, the designed principle of the compact circular phase-shift feeding network mainly depends on its two essential features: the first point is to shrink the antenna array by compressing the feeding line. The other point is the effect of the feeding network on the CP bandwidth.

3.1. Investigation of compact circular phase-shift feeding network

Fig. 10(a) illustrates the configuration of the feeding network that is printed on the F4B substrate (the relative permittivity $\varepsilon_r = 3$, the loss tangent tan $\delta = 0.003$, and thickness is 0.5 mm). The feeding port is located at the center of the substrate which is connected with ports 2 and 4 by the $\lambda_g/4$ and $3\lambda_g/4$ folded rectangular microstrip lines (λ_g is equal to 40.2 mm at the center frequency of 4.8 GHz), respectively. To further match the input impedance, the corner-truncated technique is adopted. In addition, double 90° circular arcs with inner radius $r = 6$ mm connect ports 2 and 4 with ports 3 and 5, respectively. To further clarify the mechanism of a compact circular feeding network, the simple equivalent circuit model (neglecting the coupling effect of folded lines) can be seen in Fig. 10(b). Ports 2 and 4 with impedance $Z_0 = 50$ Ω link to ports 3 and 5 by the $\lambda_g/4$ microstrip lines with the characteristic impedance $Z_2 = 59.14$ Ω, which can attain a 90° phase difference between ports 2, 4, and ports 3,5, respectively. Furthermore, the impedance of $Z_1 = 54$ Ω is for the paths $\lambda_g/4$ and $3\lambda_g/4$ each connecting the feeding port 1 with ports 2 and 4 to acquire better impedance matching between the input and output ports. Simultaneously, the sequential phases of 0°, 90°, 180°, and
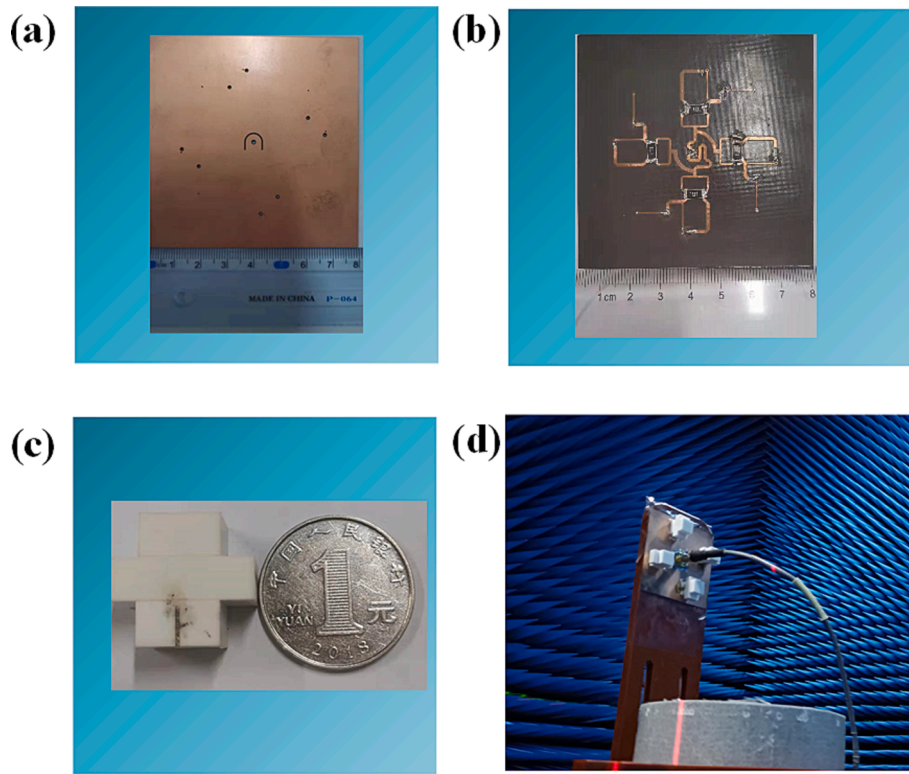
Fig. 15. (a) The top surface of substrate in the DRA array. (b) The bottom surface of substrate in the DRA array. (c) The diagram of cross-shaped DR. (d) Measurement of DRA array in anechoic chamber.
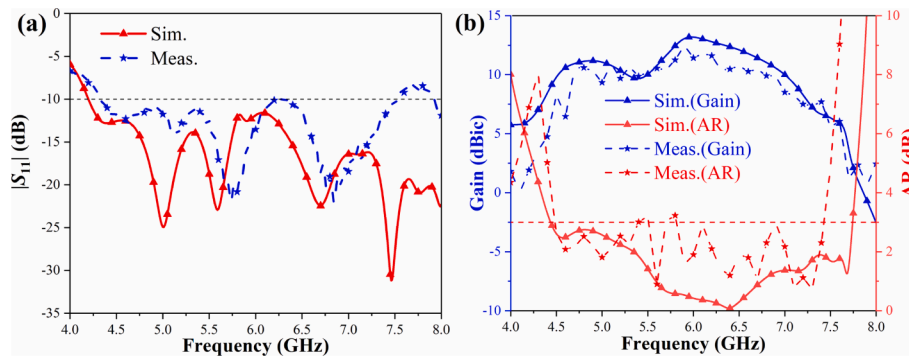

Fig. 16. The simulated and measured results of CP DRA array. (a) Reflection coefficients $|S_{11}|$. (b) Gain and AR.

270° can be achieved by creating different paths mentioned above. The detailed sizes of the feeding network can be seen in Table 3.

To clarify the scattering and phase characteristics of the feeding network, the numerical simulation is performed by the commercial software HFSS, as depicted in Fig. 11(a) and (b). As port 1 is excited, the IMB of the feeding network covers 4.25–5.5 GHz, where the transmission coefficients of different output ports are all above −7 dB. The phase difference of 90°±10° between ports 2 and 3 is mainly located at 4.5–5.5 GHz, and that between ports 4 and 5 concentrates on 4.2–5.2 GHz, which both vary linearly with the frequency. However, the phase difference between ports 3 and 4 can keep nearly 90°±10° at 4–6.1 GHz. The phase difference stability in a wide band mainly contributes to the coupling effects between the adjacent folded microstrip lines, which will introduce the parasitic capacitance whose value varies nonlinearly with the frequency and further causes the nonlinear change of the electrical length. Therefore, the phase differences between the adjacent ports all can keep nearly 90° in the 4.5–5.2 GHz, which are located in the IMB of 4.25–5.5 GHz.

However, the narrow IMB of the initial circular phase shifter still cannot support the broadband DRA array. To overcome this limitation, the different slots (circular, C-shaped, and U-shaped) are etched on the ground, respectively, which can introduce the additional capacitance to counteract the inductive effect of the feeding probe. Meanwhile, the slots also can induce new resonances in the high-frequency band, which is close to the resonant frequency of DR to further extend the IMB of DRA array. It can be noted in Fig. 11(c) that the added circular slot cannot effectively extend the IMB, but the C-shaped slot can induce the other magnetic resonance in the high frequency band to further extend the operating bandwidth of the shifter to 4–7.1 GHz, which is similar to that of the phase shifter with the U-shaped slot, 4.06–7.36 GHz. Considering the IMB and fabrication comprehensively, the U-shaped slot is finally selected to be introduced to the compact circular phase shifter, whose scattering parameters are depicted in Fig. 11(d). Note that the transmission coefficients from the port 1 to different output ports are almost above −7 dB in most of the operating band except around 5.4 GHz and the high-frequency band ($|S_{31}|$ will deteriorate around 6 GHz due to the
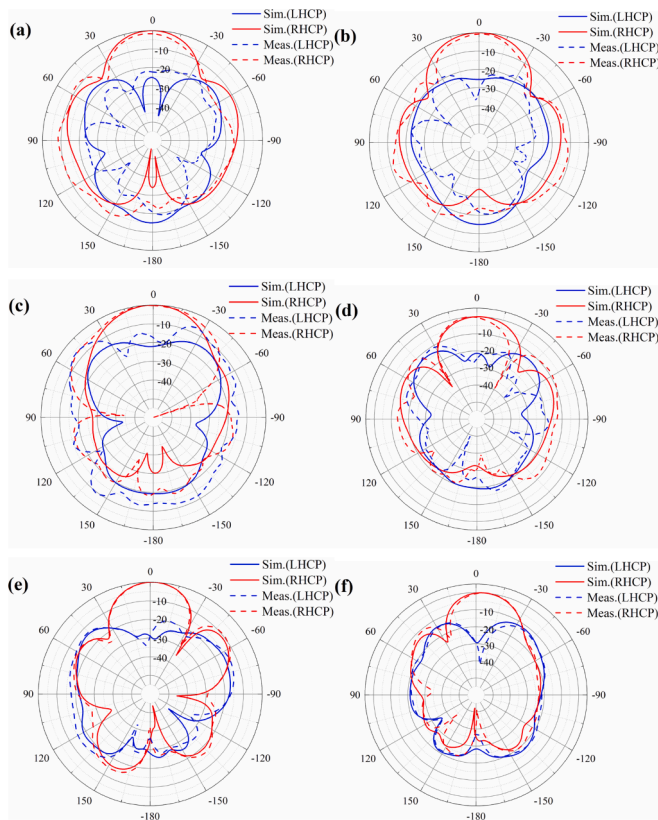
Fig. 17. The simulated and measured normalized radiation patterns in XOZ and YOX planes at different frequencies. (a) XOZ plane at 4.5 GHz. (b) YOZ plane at 4.5 GHz. (c) XOZ plane at 5.5 GHz. (d) YOZ plane at 5.5 GHz. (e) XOZ plane at 6.5 GHz. (a) YOZ plane at 6.5 GHz.

coupling effect of folded microstrip lines), which satisfies the requirement of the CP DRA array.

3.2. Discussion of CP DRA array

Four units of CP DRAs (depicted in Fig. 1(a)) are combined based on the compact circular phase-shift feeding network without the slot (shown in Fig. 10(a)) to fabricate the 2 × 2 CP DRA array (80 mm × 80 mm × 20 mm) (presented in Fig. 12).According to the simulation results (shown in Fig. 13), the IMB of the DRA array covers 4.26–6.63 GHz (43.26 %) and the 3-dB AR bandwidth ($\theta = 0°$) is located at 4.44–7.74 GHz (54.2 %). Therefore, the effective bandwidth ($|S_{11}|<$-10 dB and AR < 3 dB) is 4.44–6.63 GHz (39.6 %), where the gain ($\theta = 0°$) is above 10 dBic and the peak gain can reach 13.2 dBic at 6 GHz. After the introduction of the U-shaped slot, the DRA array can achieve the IMB of 4.2–8.11 GHz (63.5 %) and 3-dB AR bandwidth of 4.12–7.68 GHz (60.3 %), which means that the effective bandwidth can reach 4.2–7.68 GHz (58.6 %). Meanwhile, it can be noted that the U-shaped slot has a negligible effect on the gain in the low band, but slightly deteriorates the gain around 7.45 GHz. Simultaneously, the electric-field distribution in the proposed ameliorated DRA array at 4.5 GHz is also calculated to verify the phase-shift characteristic of the proposed circular phase shifter and the RHCP mechanism of the DRA array, as presented in Fig. 14. Observe that the excited field (the rotation of its electric-field vector pattern) by the compact circular phase shifter is rotationally transmitted to the next one in one quarter of the time period T. In other words, the all adjacent DRs are excited with 90° phase difference to further acquire the RHCP radiation.

4. Measurement and discussion

To verify the mechanism and designed details, an experimental prototype of the CP DRA array (shown in Fig. 15) has been fabricated and measured. The copper (thickness of 0.03 mm) microstrip feeding network and ground with U-shaped slot are printed on the bottom and top of 80 mm × 80 mm × 0.5 mm F4B with permittivity of 3, respectively. To avoid connecting the feeding probe and ground, the drilled holes for the probe should be larger than the diameter of probes, as illustrated in Fig. 15(a). Furthermore, four 50-Ω resistances are welded on the feeding network on the bottom of F4B, as depicted in Fig. 15(b).

Table 4
Comparison between our CP DRA ARRAY with reported CP DRAs.

Ref.	ε_r	Size ($\lambda_0 \times \lambda_0 \times \lambda_0$)	3-dB AR Bandwidth (%)	IMB (%)	Peak Gain (dBic)	Element number	Polarization
[25]	8.9	$0.7 \times 0.7 \times 0.158\lambda_0^3$	5.1–8.2 GHz (47.69 %)	5–8.15 GHz (48.46 %)	6.4	1 element	RHCP
[26]	12	$0.79 \times 0.79 \times 0.103\lambda_0^3$	4.75–8 GHz (54.1 %)	4.4–8 GHz (60 %)	4.55	1 element	RHCP
[28]	9.8	$0.51 \times 0.51 \times 0.21\lambda_0^3$	2.75–3.52 GHz (24.6 %)	2.82–3.83 GHz (30.37 %)	5.5	1 element	LHCP
[29]	10	$0.484 \times 0.484 \times 0.237\lambda_0^3$	3.72–6.53 GHz (54.8 %)	3.71–7.45 GHz (66.8 %)	4.68	1 element	LHCP
[30]	9.8	$0.39 \times 0.39 \times 0.15\lambda_0^3$	2.21–2.48 GHz (54.84 %)	2.17–3.81 GHz (11.53 %)	5.9	1 element	RHCP
[31]	10	$0.50 \times 0.44 \times 0.42\lambda_0^3$	3.68–5.80 GHz (44.73 %)	2.9–6.0 GHz (69.66 %)	6.34	1 element	RHCP
[32]	9.2	$0.427 \times 0.427 \times 0.244\lambda_0^3$	1.83–2.85 GHz (43.5 %)	–	7.7	1 element	RHCP/ LHCP
[35]	10.2	$2.13 \times 2.13 \times 0.135\lambda_0^3$	9–11.7 GHz (26 %)	8–12.5 GHz (44 %)	12	2 × 2 elements	RHCP
[36]	10.2	$1.6 \times 1.096 \times 0.158\lambda_0^3$	8.35–12.2 GHz (38.5 %)	8–12.3 GHz (43 %)	10.5	2 × 2 elements	RHCP
[37]	9.8	$1.57 \times 0.809 \times 0.12\lambda_0^3$	4.5–5.7 GHz (23.52 %)	4.7–6.4 GHz (30.9 %)	10	1 × 4 elements	RHCP
[39]	10.2	–	55–64.5 GHz (15.9 %)	50–67 GHz (29 %)	11.43	2 × 2 elements	LHCP
Element in this work	9.5	$0.59 \times 0.59 \times 0.29\lambda_0^3$	5.57–7.86 GHz (34.1 %)	4.43–5.11 GHz, 6.16–6.68 GHz (14.2 % and 8.1 %)	7.4	1 element	RHCP
Array in this work	9.5	$1.17 \times 1.17 \times 0.29\lambda_0^3$	4.5–7.4 GHz (48.7 %)	4.37–7.54 GHz (53.2 %)	12.48	2 × 2 elements	RHCP

(λ_0 is the wavelength in air at lowest operating frequency. "-" refers to the parameter that is not given.).

Meanwhile, the four cross-shaped DR made of ceramics with permittivity of 9.5 are tailored, where double small copper patches are printed, as shown in Fig. 15(c). Finally, the feeding probes are welded on the feeding network, and simultaneously to ensure the connection between the feeding probes and patches on the DR, a thin tin are also soldered to connect the probes and patches.

The scattering parameters are tested with the vector network analyzer (Keysight E5071C) and the radiated characteristics are measured in the anechoic chamber (illustrated in Fig. 15 (d)). It can be seen in Fig. 16(a) that the measured IMB covers 4.37–7.54 GHz (53.2 %), which is reduced by 10.3 % compared to the simulation result. In addition, the measured 3-dB AR bandwidth of 4.5–7.4 GHz (48.7 %), as depicted in Fig. 16(b), is also lower by 11.6 % than the simulation. Therefore, the effective bandwidth of the CP DRA array is located at 4.5–7.4 GHz (48.7 %), which is also reduced by 9.9 %. Simultaneously, the 10-dBic gain bandwidth is 4.7–7 GHz (39.3 %) and the peak gain can reach 12.48 dBic, as presented in Fig. 16(b). The slight deterioration is due to the added soldering tin existing between the probe and conducting patch on the DR, which may affect the impedance matching between the DR and feeding network, and produce extra power loss. Meanwhile, since the eight feeding probes are manually welded into the feeding network, it is impossible to ensure that the welding situations of each feeding probe are consistent, e.g., slightly deviating from the vertical direction, the solder slightly padding up the probes, etc., thus leading to a certain difference in the effective contacting length between the eight feeding probes and the DRs. Furthermore, the slight difference of effective contacting length can cause a mild change in the phase difference between the adjacent output ports compared with the simulation, which makes it possible that the 3-dB AR bandwidth deteriorates slightly compared to the ideal result of simulation. Additionally, the tolerance of fabrication of DR and feeding network is also responsible for the mild deterioration of DRA array performance.

Based on the CP antenna testing system in the anechoic chamber, the CP radiation patterns of the designed CP DRA array at different frequencies can be measured. It can be noted in Fig. 17 that the measured radiation patterns are similar to the simulated ones, which can verify the accuracy of measurement. In the broadside direction ($\theta = 0°$), the simulated isolation between the RHCP and LHCP both can reach 25.5 dB in XOZ and YOZ planes at 4.5 GHz (22.5 dB and 21.4 dB in XOZ and YOZ planes at 5.5 GHz, and 29.9 dB and 27.5 dB in XOZ and YOZ planes at 6.5 GHz, respectively). Based on the measurement results, the RHCP fields are higher by 20.4 dB and 29.7 dB than the LHCP ones in XOZ and YOZ planes at 4.5 GHz, respectively, (17.3 and 24 dB at 5.5 GHz, and 32.5 and 41.3 dB at 6.5 GHz) in the broadside direction. Meanwhile, the angle of the broadside direction ($\theta = 0°$) where the RHCP fields of the DRA array dominate over LHCP ones can reach 53.8° and 56.3° in XOZ and YOZ planes at 4.5 GHz according to simulation results (35.8° and 41° at 5.5 GHz, and 43.1° and 28.7° at 6.5 GHz), respectively. The measured RHCP angle can reach 46.4° and 43.5° in XOZ and YOZ planes at 4.5 GHz (40.2° and 35° at 5.5 GHz, and 40.9° and 30.8° at 6.5 GHz), respectively.

Table 4 summarizes and compares the characteristics of CP DRA based on the DRs with the similar permittivity including this work and other reported CP DRAs in terms of size, 3-dB AR bandwidth, IMB, peak gain, element, and polarization. Compared with the reported one-element DRA[25,26,28–32], the proposed DRA element in this work can achieve the higher gain of 7.4 dBic with double CP bands. Although the increase of number in the reported 2 × 2 DRA arrays without external auxiliary structures [36,37,39], e.g., reflector, EBG, cavity, etc., can effectively raise the gain, their single method of acquiring the CP radiation still limits their CP bandwidth. However, the designed DRA array in this paper attain the ultrabroad AR bandwidth by utilizing the double-point feeding structure and circular phase shifter while maintaining the higher gain based on the stacked configuration and the element coupling. Meanwhile, the compact feeding network also contributes to shrinking the horizontal size of the DRA, which is beneficial

to the further integration application. Compared to the CP MPA arrray with the identical element number[38,51–53], the proposed DRA array will achieve the higher gain by about 3–4 dBic, which means the antenna can cover a larger area that is vital for the 5G communication system. In addition, the 2 × 2 DRA array also can be regarded as the basic element to fabricate the DRA array with more elements by utilizing the appropriate feeding network, which can show better antenna performance, e.g., higher gain, wider CP bandwidth, *et al.*, in the 5G communication system.

5. Conclusion

This paper proposes an ultra-broadband CP DRA array based on Al_2O_3 ceramic with the small horizontal size working in the C-band for 5G communication. Al_2O_3 ceramic has made a constructive contribution to the performance enhancement and stability of the DRA. A series of feeding structures consisting of multiple units of double-point feeding networks and compact circular phase-shift feeding structures are tailored to excite the cross-shaped DRs, which greatly extends the 3-dB AR bandwidth and reduces the sizes of the 2 × 2 DRA array. Meanwhile, the stacking structure of DR can induce multiple Mie resonances to further improve the antenna gain. Measured results show that the DRA array with the horizontal size of $1.17 \times 1.17 \, \lambda_0^2$ can attain the 3-dB AR bandwidth of 48.7 %, IMB of 53.2 %, and peak gain of 12.48 dBic. The characteristics of the proposed DRA array indicate that it is an excellent candidate for 5G communication systems.

Declaration of Competing Interest

The authors declare that they have no known competing financial interests or personal relationships that could have appeared to influence the work reported in this paper.

References

[1] R.W.Z. Lin, T.C. Baum, 28 GHz compact omnidirectional circularly polarized antenna for device-to-device communications in the future 5G systems, IEEE Trans. Antennas Propag. 65 (2017) 6904–6914.

[2] S. Rappaport, Y. Xing, G.R. MacCartney, A.F. Molisch, E. Mellios, J. Zhang, Overview of millimeter wave communications for fifth generation (5G) wireless networks-with a focus on propagation models, IEEE Trans. Antennas Propag. 65 (2017) 6213–6230.

[3] W. Hong, Solving the 5G mobile antenna puzzle: Future directions for the 5G mobile antenna paradigm shift, IEEE Micro. Mag. 18 (2017) 86–102.

[4] W. Hong, Z.H. Jiang, C. Yu, J. Zhou, P. Chen, Z. Yu, H. Zhang, B. Yang, X. Pang, M. Jiang, Y. Cheng, M.K.T. Al-Nuaimi, Y. Zhang, J. Chen, S. He, Multibeam antenna technologies for 5G wireless communications, IEEE Trans. Antennas Propag. 65 (12) (2017) 6231–6249.

[5] K. Carver, J. Mink, Microstrip antenna technology, IEEE Trans. Antennas Propag. 29 (2003) 2–24, https://doi.org/10.1109/TAP.1981.1142523.

[6] Y. Sung, Bandwidth enhancement of a microstrip line-fed printed wide-slot antenna with a parasitic center patch, IEEE Trans. Antennas Propag. 60 (4) (2012) 1712–1716.

[7] R. S. Yaduvanshi, H. Parthasarathy. Rectangular dielectric resonator antennas, Springer, (2016).

[8] K.M. (Kwai M. Luk, K.W. (Kowk W. Leung, Dielectric resonator antennas, (2003).

[9] A. Petosa, Dielectric Resonator Antenna Handbook, Artech House, Norwood, MA, U.S.A, 2007.7.

[10] K.W. Li, strip-fed rectangular dielectric resonator antennas with/without a parasitic patch, IEEE Trans. Antennas Propag. 53 (7) (2005) 2200–2207.

[11] K.K. Dash, T. Khan, Y.M.M. Antar, A state-of-art review on performance improvement of dielectric resonator antennas, Int. J. RF MICROW. c. e. 28 (2018) 21270.

[12] R. Meher, B.R. Behera, S.K. Mishra, A.A. Althuwayb, A chronological review of circularly polarized dielectric resonator antenna: Design and developments, Int. J. RF MICROW. c. e. 31 (2021) 22589.

[13] H.T. Haneishi, Broadband circularly polarized planar array composed of a pair of dielectric resonator antennas, Electron. Lett 21 (n.d.) (1985) 437–438.

[14] A. Petosa, Ittipiboon, array of circular-polarized cross dielectric resonator antennas, Electron. Lett 32 (1996) 1742–1743.

[15] K. Tam, R.D. Murch, Circularly Polarized circular sector dielectric resonator antenna, IEEE Trans. Antennas Propag. 48 (2002) 126–128.

[16] R. Chair, S.L.S. Yang, A.A. Kishk, K.F. Lee, K.M. Luk, Aperture fed wideband circularly polarized rectangular stair shaped dielectric resonator antenna, IEEE Trans. Antennas Propag. 54 (4) (2006) 1350–1352.

[17] G. Varshney, S. Gotra, V.S. Pandey, R.S. Yaduvanshi, Inverted-sigmoid shaped multiband dielectric resonator antenna with dual-band circular polarization, IEEE Trans. Antennas Propag. 66 (4) (2018) 2067–2072.

[18] R. Chowdhury, R.K. Chaudhary, Investigation on different forms of circular sectored-dielectric resonator antenna for improvement in circular polarization performance, IEEE Trans. Antennas Propag. 66 (10) (2018) 5596–5601.

[19] N.N. Kumar, R.K. Chaudhary, A new dual C-shaped rectangular dielectric resonator based antenna for wideband circularly polarized radiation, Int. J. RF MICROW. c. e. 29 (2018) 21672.

[20] Y. Huang, J.Y. Wu, K.L. Wong, Cross-slot-coupled microstrip antenna and dielectric resonator antenna for circular polarization, IEEE Trans. Antennas Propag. 47 (1999) 605–609.

[21] L.-X. Li, S.-S. Zhong, S.-Q. Xu, M.-H. Chen, Circularly polarized ceramics dielectric resonator antenna excited by Y-shaped microstrip, Micro. Opt. Techn. Let. 51 (10) (2009) 2416–2418.

[22] S.K. Khamas, Circularly polarized dielectric resonator antenna excited by a conformal wire, Antennas Wirel. Propag. Lett. 7 (2008) 240–242.

[23] E.H. Lim, K.W. Leung, X.S. Fang, The compact circularly-polarized hollow rectangular dielectric resonator antenna with an underlaid quadrature coupler, IEEE Trans. Antennas Propag. 59 (1) (2011) 288–293.

[24] G. Massie, M. Caillet, M. Clenet, Y.M.M. Antar, A new wideband circularly polarized hybrid dielectric resonator antenna, IEEE Antenn. Wirel. PR. 9 (2010) 347–350.

[25] S.Z. Han J. Liu Design of Circularly-polarized Dielectric Resonator Antenna with Wideband Feed Network in: Proceedings of 2014 3rd Asia-Pacific Conference on Antennas and Propagation 2014.

[26] S.Z. Han, J. Liu, Wideband circularly-polarized dielectric resonator antenna with sequentially rotated feed, In: 2014 IEEE Antennas and Propagation Society International Symposium (2014).

[27] R. Kumari, R.K. Gangwar, circularly polarized cylindrical dielectric resonator antenna excited by dual conformal strips along with modified wilkinson power divider for high gain application, Microw. Opt. Tech. Lett. 59 (4) (2017) 908–913.

[28] R. Chowdhury, N. Mishra, M.M. Sani, R.K. Chaudhary, Analysis of a wideband circularly polarized cylindrical dielectric resonator antenna with broadside radiation coupled with simple microstrip feeding, IEEE Access 5 (2017) 19478–19485.

[29] M.K. Abedian, V. Singh, P. Xiao, R. Tafazolli, A.A. Kishk, Novel wideband circularly polarized DRA with squint-free radiation characteristics, Sci. Rep. 11 (2021) 7198.

[30] R. Kumar, R.K. Chaudhary, Stacked rectangular dielectric resonator antenna with different volumes for wideband circular polarization coupled with step-shaped conformal strip, Int. J. RF. Microw. c. e. 29 (2019) 1–8.

[31] S. Trinh-Van, Y. Yang, K.-Y. Lee, K.C. Hwang, Single-fed circularly polarized dielectric resonator antenna with an enhanced axial ratio bandwidth and enhanced gain, IEEE Access 8 (2020) 41045–41052.

[32] S. Liu, D. Yang, Y. Chen, S. Huang, Y. Xiang, Broadband dual circularly polarized dielectric resonator antenna for ambient electromagnetic energy harvesting, IEEE Trans. Antennas Propag. 68 (6) (2020) 4961–4966.

[33] D. Gupta, M.S. Parihar, Differentially fed wideband rectangular DRA with high gain using short horn, IEEE Antenna. Wirel. P. L. 16 (2017) 1804–1807.

[34] M.J. Al-Hasan, T.A. Denidni, A.R. Sebak, Millimeter-wave EBG-based aperture-coupled dielectric resonator antenna, IEEE Trans. Antennas Propag. 61 (8) (2013) 4354–4357.

[35] S.-L. Yang, R. Chair, A.A. Kishk, K.-F. Lee, K.-M. Luk, Study on sequential feeding networks for subarrays of circularly polarized elliptical dielectric resonator antenna, IEEE Trans. Antennas Propag. 55 (2) (2007) 321–333.

[36] M.I.A. Mahmoud, G. Varshney, A.A. Ibrahim, An array of staircase-shaped circularly polarized DRA, Int. J. RF Micro. c. e. 31 (2021).

[37] S. Gupta, A. Sharma, G. Das, R.K. Gangwar, M. Khalily, Wideband circularly polarized dielectric resonator antenna array with polarization diversity, IEEE Access 7 (2019) 49069–49076.

[38] W.-W. Yang, W.-J. Sun, H. Tang, J.-X. Chen, Design of a circularly polarized dielectric resonator antenna with wide bandwidth and low axial ratio values, IEEE Trans. Antennas Propag. 67 (3) (2019) 1963–1968.

[39] Y.-X. Sun, K.W. Leung, Circularly polarized substrate-integrated cylindrical dielectric resonator antenna array for 60 GHz applications, Antennas Wirel. Propag. Lett. 17 (8) (2018) 1401–1405.

[40] N. Chen, J.M. Song, J.D. Park, A compact circularly polarized MIMO dielectric resonator antenna over electromagnetic band-gap surface for 5G applications, IEEE Access 7 (2019) 140889–140898.

[41] M. Rad, N. Nikkhah, B. Zakeri, M. Yazdi, Wideband dielectric resonator antenna with dual circular polarization, IEEE Trans. Antennas Propag. 70 (1) (2022) 714–719.

[42] K.X. Song, S.Y. Wu, X.M. Chen, Effects of Y_2O_3 addition on microwave dielectric characteristics of Al_2O_3 ceramics, Mater. Lett. 61 (16) (2007) 3357–3360.

[43] S.J. Penn, N.M. Alford, A. Templeton, X.R. Wang, M.S. Xu, M. Reece, K. Schrapel, Effect of porosity and grain size on the microwave dielectric properties of sintered alumina, J. Am. Ceram. Soc. 80 (1997) 1885–1888.

[44] N.M.N. Alford, S.J. Penn, Sintered alumina with low dielectric loss, J. Appl. Phys. 80 (1996) 5895–5898.

[45] Z. Wang, L. Liu, Q. Du, RuiTao Tang, J. Ai, Y. Chen, Enhanced microwave dielectric properties of CeO_2–TiO_2 ceramics by adding Al_2O_3 for microstrip antenna application, Ceram. Int. 48 (10) (2022) 14378–14385.

[46] Q.i. Yuan, H. Ma, J. Jiang, J. Wang, Y. Li, S. Zhao, S. Qu, Al_2O_3 based ceramic with polarization controlled meta-structure for high-temperature broadband backward scattering manipulation, J. Alloy. Compd. 854 (2021) 157168.

[47] M. Samsuzzaman, M.T. Islam, J.S. Mandeep, Parametric analysis of a glass-micro fibre-reinforced PTFE material, multiband, patch-structure antenna for satellite applications, J. Optoelectron. Adv. m. 7 (2015) 760–769.

[48] M. Deja, D. Zieliński, Wear of electroplated diamond tools in lap-grinding of Al_2O_3 ceramic materials, Wear 460-461 (2020) 203461.

[49] M.H. Ullah, M.T. Islam, Design of a modified W-shaped patch antenna on Al_2O_3 ceramic material substrate for Ku-band, Chalcogenide Lett. 9 (2012) 61–66.

[50] S.B. Narang, S. Bahel, Low loss dielectric ceramics for microwave applications: a review, J. Ceram. Process. Res. 11 (2010) 316–321.

[51] B. Mukherjee, P. Patel, J. Mukherjee, A review of the recent advances in dielectric resonator antennas, J. Electromagnet. Wave. 34 (2020) 1095–1198.

[52] W.-J. Sun, W.-W. Yang, P. Chu, J.-X. Chen, Design of a wideband circularly polarized stacked dielectric resonator antenna, IEEE Trans. Antennas Propag. 67 (1) (2019) 591–595.

[53] Y. Zhang, N.W. Liu, J.Y. Zhao, G. Fu, Wideband circularly polarized antenna with gain improvement, IEEE Antennas Wirel. P. L. 12 (2013) 456–459.